Symmetric projected entangled-pair states analysis of a phase transition in coupled spin-$\frac{1}{2}$ ladders

Juraj Hasik [1,2,*] Glen Bigan Mbeng,[3] Sylvain Capponi,[2] Federico Becca,[4] and Andreas M. Läuchli [5,6,3]

[1]*Institute for Theoretical Physics, University of Amsterdam, Science Park 904, 1098 XH Amsterdam, Netherlands*
[2]*Laboratoire de Physique Théorique, Université de Toulouse, CNRS, UPS, Toulouse, France*
[3]*Institut für Theoretische Physik, Universität Innsbruck, A-6020 Innsbruck, Austria*
[4]*Dipartimento di Fisica, Università di Trieste, Strada Costiera 11, I-34151 Trieste, Italy*
[5]*Laboratory for Theoretical and Computational Physics, Paul Scherrer Institute, 5232 Villigen, Switzerland*
[6]*Institute of Physics, École Polytechnique Fédérale de Lausanne (EPFL), 1015 Lausanne, Switzerland*

Infinite projected entangled-pair states (iPEPS) have been introduced to accurately describe many-body wave functions on two-dimensional lattices. In this context, two aspects are crucial: the systematic improvement of the *Ansatz* by the optimization of its building blocks, i.e., tensors characterized by bond dimension D, and the extrapolation scheme to reach the "thermodynamic" limit $D \to \infty$. Recent advances in variational optimization and scaling based on correlation lengths demonstrated the ability of iPEPS to capture phases with spontaneously broken continuous symmetry such as the antiferromagnetic (Néel) one with high fidelity, in addition to valence-bond solids which are already well described by finite-D iPEPS. In contrast, systems in the vicinity of continuous quantum phase transitions still present a challenge for iPEPS, especially when non-Abelian symmetries are involved. Here, we consider the iPEPS *Ansatz* to describe the continuous transition between the (gapless) antiferromagnet and the (gapped) paramagnet that exists in the $S = 1/2$ Heisenberg model on coupled two-leg ladders. In particular, we show how accurate iPEPS results can be obtained down to a narrow interval around criticality and analyze the scaling of the order parameter in the Néel phase in a spatially anisotropic situation.

I. INTRODUCTION

One of the most challenging problems in condensed matter theory is to obtain sufficiently accurate approximations of the ground state and low-energy excitations of generic many-body Hamiltonians. For this reason, several numerical approaches have been devised in the last 30 years, including density-matrix renormalization group (DMRG) [1], dynamical mean-field theory [2], and quantum Monte Carlo (QMC) techniques [3]. In particular, DMRG has become the reference method to address strongly correlated systems in one spatial dimension. Its reformulation by using the so-called matrix-product states [4,5] has led to straightforward generalizations to two-dimensional systems; in this regard, projected entangled-pair states (PEPS) [6,7] represent a promising computational framework to obtain accurate results on generic lattice models. Within this approach, the ground-state wave function is represented by means of local tensors, typically assigned the sites of the underlying lattice. These tensors have two kinds of indices: a single *physical* index specifying the local physical configuration (e.g., $S^z = \pm 1/2$ in a spin-1/2 model) and a collection of auxiliary *bond* indices (whose number, usually, equals the coordination number of the lattice), each one having bond dimension D. The bond indices on nearest-neighbor sites are contracted together, thus defining

a *tensor network*. The accuracy of these wave functions can be systematically improved by raising the bond dimension. Furthermore, infinite systems may be considered by embedding the tensor network within a suitable environment. Such tensor networks, dubbed iPEPS, are the main focus of this work.

In the last decade, several algorithms to optimize iPEPS *Ansätze* have been developed and used to address challenging problems in different correlated systems, ranging from the characterization of unconventional states of matter (e.g., spin liquids in the highly frustrated spin model) to the competition between stripes and superconductivity in Hubbard or *t-J* models. For example, the ground-state of the spin-$\frac{1}{2}$ Heisenberg model has been analyzed on the kagome [8] and Shastry-Sutherland [9] lattices. Hamiltonians with an enlarged $SU(N)$ "spin" symmetry have been also considered, to assess both magnetically ordered and disordered phases [10,11]. In this regard, particular attention has been devoted to the possibility to stabilize chiral spin liquids [12,13]. As far as electronic models are concerned, the evidence in favor of stripes has been pushed for *t-J* [14] and Hubbard [15] models, in the vicinity of the hole doping $\delta = 1/8$.

The iPEPS *Ansatz* is particularly suited to describe phases with a gap in the excitation spectrum. In this case, very accurate or even exact ground-state wave function can be obtained already for finite (and often relatively small) bond dimension D. Instead, gapless phases (most notably, magnetically ordered phases with Goldstone modes, but also states corresponding to quantum critical points) can be captured

*j.hasik@uva.nl

only approximately, with the exact description obtained in the limit $D \to \infty$. This is in stark contrast with what happens in one spatial dimension, where tensor-network states, equipped with an appropriate scaling theory, may capture very well gapless phases and critical phenomena [16–19]. Recently, progress in the iPEPS analysis of critical and/or gapless systems has been made thanks to two key developments. The first one is the introduction of optimization techniques, based either on diagram summations [20,21] or the so-called automatic differentiation [22], which substantially improve the accuracy with respect to the commonly used imaginary time evolution methods. The second one is the development of finite-correlation-length scaling (FCLS) [23,24] that allowed leveraging the well-established finite-size scaling approach to iPEPS states. In effect the accuracy of thermodynamic estimates based on finite-D iPEPS calculations can be considerably improved. The efficiency of these advances was recently demonstrated on a paradigmatic problem of the spin-$\frac{1}{2}$ Heisenberg J_1-J_2 model on a square lattice by estimating the magnetization curve within the Néel phase, even in the vicinity of the transition to the quantum spin-liquid state [25].

In this work, we pursue the idea of describing a continuous phase transition within the iPEPS formalism. In particular, as for the J_1-J_2 model, we focus on a case where the Néel order is melted by quantum fluctuations, namely a two-dimensional system of coupled spin-1/2 Heisenberg ladders defined by

$$\mathcal{H} = J \sum_R \mathbf{S}_R \cdot \mathbf{S}_{R+\hat{x}} + \sum_R J_R \mathbf{S}_R \cdot \mathbf{S}_{R+\hat{y}}, \tag{1}$$

where $\mathbf{S}_R = (S_R^x, S_R^y, S_R^z)$ is the $S = 1/2$ operator on the site $R = (x, y)$ of a square lattice, $\hat{x}$ and $\hat{y}$ are unit vectors in x and y directions, and $J_R = J$ or $J_R = \alpha J$, depending on the parity of y. By varying α, this model interpolates between the Heisenberg model on the square lattice at $\alpha = 1$ and a system of decoupled two-leg ladders at $\alpha = 0$. In the following, we will take J as the energy scale. Owing to the absence of the sign problem, this system can be studied by unbiased QMC techniques and, therefore, offers an excellent benchmark for the accuracy of iPEPS to describe a nontrivial quantum phase transition, e.g., beyond the simplest case of the Ising model in transverse field. Indeed, the Hamiltonian (1) displays a quantum critical point at $\alpha_c = 0.31407(5)$, separating a gapless antiferromagnet and a gapped paramagnet [26]. The critical exponents are compatible with the ones of the classical three-dimensional $O(3)$ Heisenberg model, as expected.

A recent iPEPS investigation of this Heisenberg model [27] highlighted the difficulties faced by the unrestricted optimizations of iPEPS tensors across the phase transition. In fact, due to the unbroken $SU(2)$ symmetry in the paramagnetic side, strong finite-D effects are present, thus impeding a systematic analysis. Moreover, the optimization procedure is problematic also within the antiferromagnetic phase, where the expected $U(1)$ symmetry around the direction of the staggered magnetization is usually broken. In this work, we want to constrain the iPEPS *Ansatz* by imposing this $U(1)$ symmetry, thus limiting finite-D effect, and optimize such symmetric tensors with the automatic differentiation [22]. In addition, we extend the FCLS analysis [23,24] in situations with a spatial anisotropy, due to the presence of two length scales, since

the correlations along the spatial x and y directions will be generically different in the ground state of Eq. (1). These two improvements allow us to get accurate results for the antiferromagnetic order parameter up to the critical point, as confirmed by a direct comparison with QMC calculations. Finally, we included an external staggered magnetic field in the Hamiltonian (1), which allows us to inspect the response in the order parameter, even very close to the critical point.

II. METHODS

Here, we briefly describe the structure of the iPEPS *Ansatz* that is used to investigate the Hamiltonian (1). To account for both the antiferromagnetic order in the gapless regime and the short-range valence-bond correlations in the gapped one, we consider four rank-5 tensors $t = \{a, b, c, d\}$, each one with a physical index s (with dimension 2, suitable for $S = 1/2$ degrees of freedom) and four auxiliary indices u, l, d, r (with dimension D). These tensors are arranged in a 2×2 unit cell to tile the square lattice:

$$|\text{iPEPS}(a, b, c, d)\rangle = \qquad\qquad , \tag{2}$$

where black lines represent physical indices and grey lines (contracted) auxiliary indices.

Observables are obtained by computing effective environments with the corner-transfer matrix (CTM) method, generalized for extended unit cells [14]. The CTM method approximates the corners and half-rows/columns of the infinite tensor network, arising when computing expectation values, by a set of finite tensors $\{C, T\}$ associated with each nonequivalent site in the unit cell. The corner tensors $\{C\}$ have size $\chi \times \chi$ and half-row/column transfer tensors $\{T\}$ have size $D^2 \times \chi \times \chi$, χ being the *environment* dimension. These environment tensors are then used to construct approximate reduced density matrices of finite subsystems, i.e., for nearest-neighbor sites

$$\approx \qquad\qquad , \tag{3}$$

where A, B, C, and D are double-layer tensors obtained by contracting the physical index, i.e., $A_{(uu')(ll')(dd')(rr')} = \sum_s a_{uldr}^s a_{u'l'd'r'}^{*s}$, while sites with open physical indices, $A_{(uu')(ll')(dd')(rr')}^{ss'} = a_{uldr}^s a_{u'l'd'r'}^{*s'}$, have diagonal black lines. In addition, correlation lengths of two-point functions can be computed from the spectrum of $D^2\chi^2 \times D^2\chi^2$ transfer matrices [28], such as the one above highlighted in blue once the physical indices are contracted. The CTM environments are systematically improved by increasing χ, with the exact observables recovered in the $\chi \to \infty$ limit.

The symmetries of the Hamiltonian allow us to further specialize the *Ansatz*. The gapped phase retains the full $SU(2)$ spin symmetry; by contrast, the gapless phase partially breaks this spin symmetry, leading to a finite collinear magnetization and a residual $U(1)$ symmetry about it. Therefore, we impose an explicit $U(1)$ spin symmetry on the tensors. This can be achieved by associating integer "charges" to the two physical spin-1/2 components and the D virtual degrees of freedom (on each of the bond indices) [29]. To preserve point-group symmetries of the underlying lattice, a straightforward choice is to take the same charges on all the bond indices that are equivalent under the symmetries (e.g., the choice made in Ref. [27] for a lattice with C_{4v} symmetry). Here, we do not want to impose any spatial symmetry within the 2×2 unit cell, which allows for the existence of different charges on different indices. Thus, each of the four tensors will possess a set of charges $\vec{v}_j^\gamma = (v_0, \ldots, v_{D-1})$ with $\gamma = a, b, c, d$ and $j = u, l, d, r$. Instead, the same charges $\vec{u} = (u^\uparrow, u^\downarrow)$ for the physical indices are taken for all tensors. Then, the $U(1)$ symmetry is realized by enforcing a selection rule for the nonzero elements of the tensors t_{uldr}^s:

$$u^s + v_u^\gamma + v_l^\gamma + v_d^\gamma + v_r^\gamma = N, \qquad (4)$$

where, without loss of generality, we choose the case with $N = 0$ to work with invariant tensors. From a practical point of view, one possibility of identifying $U(1)$ charges (for the best variational states) is to perform imaginary-time evolution by using a two-site simple-update scheme [30], starting from product states with $U(1)$ symmetry. Remarkably, this approach does not lead to substantial improvements (in terms of physical quantities such as energy or magnetization) with respect to the charges obtained from the unrestricted optimizations of single-site iPEPS *Ansatz* with the C_{4v} lattice symmetry in the Heisenberg model with $\alpha = 1$ [25]; see Appendix A. The use of these charges allows us to improve numerical efficiency. Tensor elements respecting the selection rule can be arranged into blocks, leading to economic block-sparse representation. For a detailed treatment of tensor networks with $U(1)$ symmetry and linear algebra with block-sparse tensors, see Ref. [29].

The optimizations of the iPEPS *Ansatz* (2) with specified $U(1)$ charges are performed by the direct minimization of the energy:

(i) The tensors a, b, c, and d are initialized and the environment tensors $\{C, T\}$ are computed, to build the reduced density matrices.

(ii) The energy per site e is computed by evaluating all eight distinct nearest-neighbor terms of Hamiltonian (1) in the 2×2 unit cell.

(iii) The gradients $\frac{\partial e}{\partial a}, \frac{\partial e}{\partial b}, \frac{\partial e}{\partial c}, \frac{\partial e}{\partial d}$ are evaluated by automatic differentiation of the entire step (ii).

(iv) The elements of tensors a, b, c, and d are then updated with the L-BFGS algorithm augmented with line search. The new environment tensors $\{C, T\}$ are computed. The optimization continues from step (ii) until the desired convergence in energy has been reached.

For details of the L-BFGS algorithm, which improves upon the simple steepest descent method, and backtracking line search used in this work, see Ref. [31]. Importantly, once

the charges are defined, the gradient optimization changes the tensor elements without mixing different symmetry-allowed blocks. The implementation of linear tensor algebra for Abelian-symmetric tensors is provided by the open-source library YAST [32], and the iPEPS algorithms built on top of it are available in the PEPS-TORCH library [33].

III. RESULTS

Let us now show the results obtained within the optimization of the iPEPS *Ansätze*. The optimizations for $D = 3, 4, 5$, and 6 are performed with environment dimensions up to $\chi = 72, 96, 100$, and 108, respectively. For each value of D the observables are then extrapolated to $\chi \to \infty$. These finite-χ corrections are generally small, at most $O(10^{-5})$ for energy and magnetization at $D = 6$ and $\alpha \to 1$, but can be sizable for correlation lengths, e.g., about 10% of the extrapolated value. Afterward, we perform FCLS analysis to obtain both $D \to \infty$ and $\chi \to \infty$ thermodynamic estimates.

To perform a careful comparison with QMC calculations (which are numerically exact, since the spin model does not suffer from the sign problem), we apply the stochastic series expansion method [34] and perform extrapolations by decreasing the temperature (to reach ground-state properties) and increasing the size of the cluster (to reach the thermodynamic limit). Most of the QMC calculations were done on $L \times L$ lattices with periodic boundary conditions, at temperature $T = 1/(2L)$, by using the ALPS libraries [35,36].

A. Phase diagram

In Fig. 1, we report the energy per site e and the staggered magnetization m^2 (averaged over the 2×2 unit cell), for different values of α across the quantum critical point. The outcome shows that for a small bond dimension (for $D \leqslant 2$ in the antiferromagnetic phase and $D \leqslant 3$ in the paramagnetic one) the accuracy is quite poor in both phases. However, once the bond dimension becomes large enough to capture the entanglement structure of the ground state, the tensor network provides an excellent variational description not only in the paramagnetic phase, where the iPEPS parametrization is particularly suitable, but also within the magnetically ordered phase. The accuracy of the ground-state energy is exemplified by showing the relative error with respect to the value e_{QMC}, obtained within the QMC approach (extrapolated in the thermodynamic limit). Indeed, the quantity $\Delta e/|e_{QMC}|$, with $\Delta e = |e - e_{QMC}|$ is vanishing within the statistical errors; see Fig. 1. Most importantly, the magnetization curves for finite values of the bond dimension D follow the QMC data faithfully in the bulk of each phase, still overestimating the order parameter close to the critical point. We would like to mention that the present QMC results allow us to locate the critical point at $\alpha_c = 0.314\,67(1)$, which is slightly different from the previous estimate $\alpha_c = 0.314\,07(5)$ [26] (see Appendix B).

B. Finite-correlation-length scaling

Obtaining accurate and reliable estimates of the observables (e.g., the energy per site or the staggered magnetization) within iPEPS *Ansätze* represents an important issue that has been addressed since their definition. Recently, a
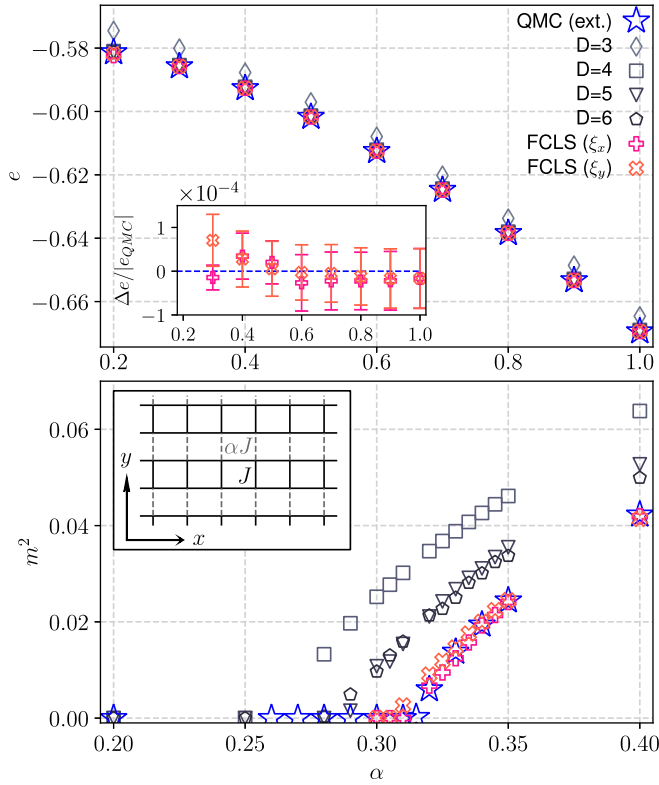
FIG. 1. Energy per site (upper panel) and staggered magnetization (lower panel) for optimized iPEPS with $U(1)$ symmetry and 2×2 unit cell. The results for $D = 3, \dots, 6$ are reported (except the magnetization for $D = 3$, which is too large), as well as the ones obtained with the FCLS extrapolation; see text. In addition, QMC results are also shown for the thermodynamic extrapolation. The inset in the upper panel shows the relative error of the iPEPS energies (with FCLS extrapolations) with respect to the QMC ones (with thermodynamic extrapolations). The inset in the bottom panel gives a sketch of the superexchanges in Hamiltonian (1), where intraladder J (interladder αJ) couplings are denoted by black solid (gray dashed) lines.

progress has been made in this direction for magnetic states that break a continuous symmetry (e.g., the antiferromagnetic one in the Heisenberg model). In this case, the presence of gapless modes induces a diverging correlation length. When working on finite clusters, as in standard QMC approaches, this fact translates into well-defined size-scaling laws of the physical quantities [37,38]. Instead, within iPEPS, we directly work in the thermodynamic limit (that is mimicked by the embedding procedure) and, therefore, it is not possible to straightforwardly apply the same scaling laws; still, the correlation length ξ is finite for any finite value of the bond dimension D and diverges with $D \to \infty$. As a result, it has been suggested [23,24] that the FCLS analysis can be defined in terms of ξ instead of the cluster size as

$$e(\xi) = e_0 + \frac{a}{\xi^3} + O\left(\frac{1}{\xi^4}\right), \tag{5}$$

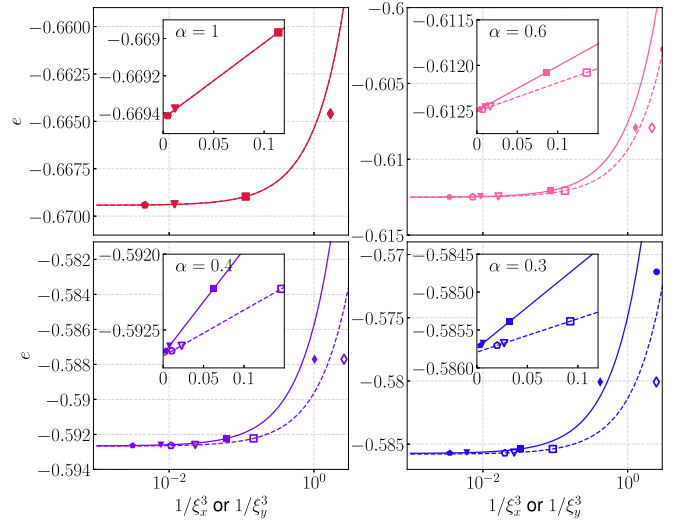$$m^2(\xi) = m_0^2 + \frac{b}{\xi} + O\left(\frac{1}{\xi^2}\right), \tag{6}$$

FIG. 2. FCLS extrapolations for the energy e, by using both horizontal (ξ_x, full symbols and lines) and vertical (ξ_y, empty symbols and dashed lines) correlation lengths, for a few values of the inter-ladder couplings α. The symbols correspond to iPEPS with $D = 3$ (diamonds), $D = 4$ (squares), $D = 5$ (triangles), and $D = 6$ (pentagons). The colors follow the α color scheme of Fig. 3.

where a and b are suitable constants. The system we are interested in, i.e., the Heisenberg model on coupled two-leg ladders, presents a complication, as it breaks the $\pi/2$-rotational symmetry for $\alpha \neq 1$, leading to two distinct length scales. Within finite-D iPEPS calculations, we have access to both of them by looking at the spectrum of the transfer matrices along x (i.e., within ladders) and y (i.e., across ladders). Thus, we obtain two correlation lengths (ξ_x and ξ_y) and perform FCLS independently for both of them. The extrapolated values e_0 and m^2 (as shown in the Fig. 1) do not depend upon the choice of the direction used to extract the correlation length, while the parameters a and b depend on the choice. It must be emphasized that these FCLS relations are expected to be valid exclusively for a phase with a spontaneously broken continuous symmetry and Goldstone modes, where the correlation length diverges with increasing D. Instead, within the paramagnetic gapped phase, ξ remains finite in the thermodynamic limit, thus implying that Eqs. (5) and (6) cannot be applied. The impossibility of fitting the numerical data for a given α within this scheme is then taken as evidence that the state is not gapless (antiferromagnetic). At the quantum critical point, we still expect Eq. (5) to hold, while the order parameter scaling is replaced with a quantum critical form $m(\xi) \approx \xi^{-\Delta_m}$, with Δ_m the scaling dimension of the order parameter at the critical point [23].

The results for the energy per site e are reported for selected values of α in Fig. 2. Within the magnetically ordered phase (but also close to the quantum critical point), the extrapolations of the FCLS analysis using either ξ_x or ξ_y give consistent values, providing an internal verification of the approach. Most importantly, the staggered magnetization m^2 can be also extracted for infinite correlation length; see Fig. 3. The extrapolated results are in very good agreement with QMC estimates, up to values of the interladder couplings that are
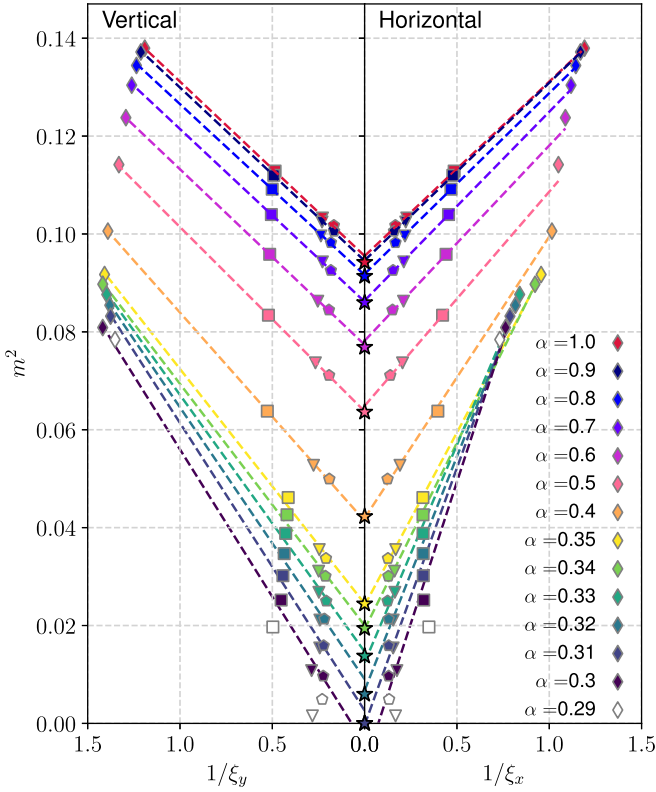
FIG. 3. FCLS extrapolations for staggered magnetization m^2, by using both vertical (ξ_y, left part) and horizontal (ξ_x, right part) correlation lengths for $0.29 \leqslant \alpha \leqslant 1$. The symbols correspond to iPEPS with $D = 3$ (diamonds), $D = 4$ (squares), $D = 5$ (triangles), and $D = 6$ (pentagons); thermodynamic extrapolations from QMC data are also reported (stars).

very close to the critical point. Beyond the critical point, the system develops a gap and thus the FCLS fails to provide the correct scaling, where correlation lengths remain finite. Nevertheless, within the paramagnetic regime, finite-D iPEPS calculations are able to recover accurate results. Indeed, for $\alpha \lesssim 0.28$, a vanishing magnetization is already obtained with $D = 5$. However, upon approaching criticality, i.e., at $\alpha = 0.3$, finite-D iPEPS retain a small residual magnetization (at least up to $D = 6$). In fact, close to the critical point, the correlation length far surpasses the values of ξ_x and ξ_y that our finite-D iPEPS can support. Hence, the FCLS analysis can be used to improve the estimates of the energy. Still, some important deviations in the scaling laws are clearly visible; see Fig. 3. Finally, let us remark that the iPEPS optimization in the narrow region near criticality is technically difficult due to the presence of instabilities (see Appendix C).

C. The effect of a staggered magnetic field

In the previous section, we focused on estimating observables of the ground state of the $SU(2)$-symmetric Hamiltonian (1). Here, we explicitly break this symmetry to investigate the phase transition with a complementary non-symmetric approach [23,39,40]. In particular, we follow the approach of Refs. [23,40], which recently used tensor networks to compute running exponents in critical quantum systems.

To explicitly break the $SU(2)$, we supplement the Hamiltonian (1) with an external *staggered* magnetic field h, which directly couples to the order parameter:

$$\mathcal{H}_h = \mathcal{H} - h \sum_R (-1)^{x+y} S_R^z, \tag{7}$$

where $R = (x, y)$. Then, for any $h \neq 0$, the ground state has a finite correlation length and develops a finite staggered magnetization $m = m(h, \alpha)$ in response to the staggered field h. The response for $h \to 0^+$ is different within magnetically ordered or disordered phases. In both cases, the magnetization is an analytic function of h, with two distinct regimes:

$$m(\alpha, h) = a(\alpha)h + O(h^2) \quad \text{for } \alpha < \alpha_c, \ h \to 0^+, \tag{8}$$

$$m(\alpha, h) = m(\alpha, 0) + O(h) \quad \text{for } \alpha > \alpha_c, \ h \to 0^+, \tag{9}$$

where $a(\alpha)$ is a suitable constant. By contrast, at criticality (i.e., for $\alpha = \alpha_c$), the magnetization is not analytic and the response follows a power-law behavior:

$$m(\alpha_c, h) \propto h^{1/\delta}, \quad \text{for } h \to 0^+, \tag{10}$$

where δ is a critical exponent, which only depends on the universality class of the phase transition. The best estimate of δ [within the expected universality class of the classical three-dimensional $O(3)$ Heisenberg model] is $1/\delta = 0.20916$ [41].

To probe the system's response at fixed α, we define the logarithmic derivative

$$[1/\delta](\alpha, h) = \frac{\partial \log m(\alpha, h)}{\partial \log h}, \tag{11}$$

which is usually referred to as *running exponent*. For each value of h, we optimize the $U(1)$-symmetric iPEPS *Ansatz* and compute the average staggered magnetization $m(\alpha, h)$. Then, we estimate the logarithmic derivative by using finite differences. The QMC results are based on a direct improved estimator for the running exponent; see Ref. [40]. The outcomes are shown in Fig. 4, where the running exponent and the correlation length ξ_x of iPEPS are reported for the three different regimes (with $D = 2, \ldots, 6$).

In the gapped phase (for $\alpha = 0.2$), the magnetization is linear in h (linear response) and, therefore, the running exponent saturates at 1 for $h \to 0$, as also obtained numerically from both QMC and iPEPS data (with $D \geqslant 4$). The iPEPS correlation length saturates for $h \lesssim 0.005$, with small finite-D corrections. Indeed, in the gapped phase, even finite-D iPEPS provide a precise description of the system, which is supported by a direct comparison between iPEPS (with $D \geqslant 4$) and QMC (for $L \geqslant 32$). The $D = 3$ iPEPS cannot faithfully capture the gapped phase at $\alpha = 0.2$, since it retains finite m and thus responds more similarly to the Néel phase.

Within the magnetically ordered phase (for $\alpha = 0.4$), the magnetization saturates to a finite value and the running exponent goes to zero for $h \to 0$. Indeed, the logarithmic derivative $[1/\delta](\alpha, h)$ has a nonmonotonic behavior, with a broad peak at intermediate values of the staggered field h. This feature is correctly captured by iPEPS. QMC calculations also reproduce the broad peak, even though at small values of h a huge upturn is present due to size effects; therefore, for
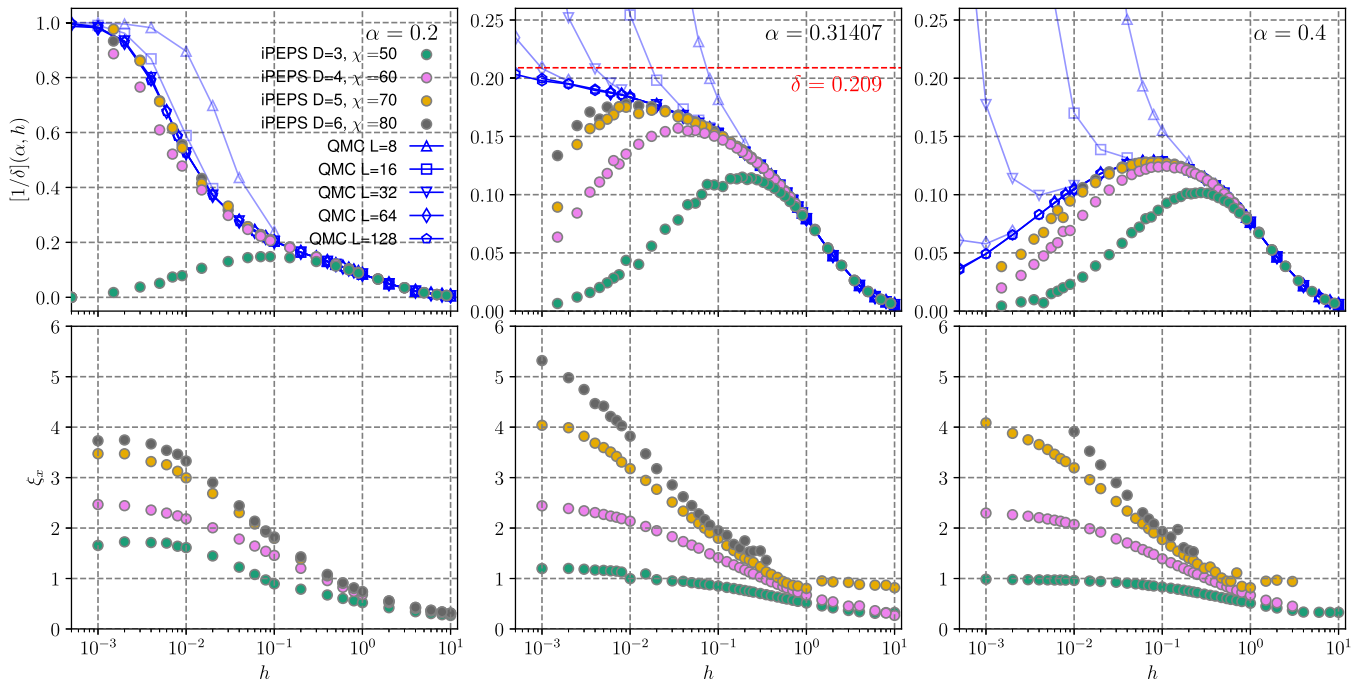
FIG. 4. $U(1)$-symmetric iPEPS with $D = 3, \ldots, 6$ in the presence of external staggered field h. Upper panels: Running exponent as a function of h for the gapped phase with $\alpha = 0.2$ (left), at criticality $\alpha = 0.31407$ (middle), and in the Néel phase $\alpha = 0.4$ (right). The value of the critical exponent $1/\delta$ is reported at the critical point. QMC results are also reported for comparison, with faded colors marking the data affected by finite lattice size. Bottom panels: horizontal correlation length ξ_x as a function of h.

a large enough system size L, the two methods converge to the same curve for sufficiently large values of the staggered field h. Here, it seems as though QMC simulations provide an upper bound of the thermodynamic limit, while iPEPS provide a lower bound of it. Still, the presence of the broad peak is robust and appears in the region of h where both $D \geqslant 5$ iPEPS and $L \geqslant 32$ QMC data are in excellent agreement.

At the critical point $\alpha = \alpha_c$, the running exponent is expected to converge towards $1/\delta = 0.209\,16$, as mentioned before. The available iPEPS and QMC calculations (for $D \leqslant 6$ and $L \leqslant 128$, respectively) are still somewhat away from the saturation regime; however, the numerical data monotonically increase, without the broad peak in the magnetically ordered phase. While the validity of the QMC results is limited by the finite size L, for iPEPS it is limited by the finite correlation length induced by the bond dimension D. Within iPEPS, as the field h is decreased, the correlation lengths initially grow, but then flatten out (with large finite-D corrections), in contrast to the expected diverging behavior of the gapless regime. From the direct comparison between QMC and iPEPS data, we can estimate that the iPEPS response for $D = 6$ gives a faithful estimation of the exact result down to $h \approx 10^{-2}$. Then, for smaller fields, the running exponent data for iPEPS and large-L QMC simulations start to deviate as iPEPS becomes increasingly biased by the induced finite correlation length.

IV. CONCLUSIONS AND OUTLOOK

The analysis of quantum phase transitions by variational methods relies on a few aspects: first, a flexible *Ansatz* for the ground-state wave function, allowing a description of different

kinds of phases by tuning its parameters; second, a practical optimization scheme of such parameters to get the best approximate ground state; finally, a way to analyze the results, possibly extrapolating to the thermodynamic limit. Here, we have shown that symmetric tensor networks, when implemented with a variational optimization, allow for an accurate description of the transition between a gapped paramagnet and a gapless Néel antiferromagnet, thus overcoming the issues arising within the imaginary-time evolution approach that was emphasized in a recent work [27]. The selection of the correct symmetry structure for tensors by the choice of their charges is crucial, as they determine the physical properties of the wave function. Most importantly, once the tensors have been variationally optimized, our simulations show that the physical observables, such as the energy or the order parameter, are robust to small variations of these charges. Although the region close to the critical point remains a challenge, it is in principle tractable by increasing the bond dimension D. Already with data up to $D = 6$ and FCSL scaling, we could locate the critical point with an accuracy of about 5%, demonstrating the applicability of this analysis even in the case of two different length scales ξ_x and ξ_y. Finally, inspired by the recent works of Refs. [23,40], we have included an external staggered field h in the Hamiltonian and compared the iPEPS results with the ones obtained by QMC. Away from the critical point $\alpha > \alpha_c$ (i.e., within the Néel phase) the running exponent $[1/\delta](\alpha, h)$ shows a broad peak at finite field h, indicative of magnetic order [40]. The robustness of the peak can be established by locating the inflection point in the growing iPEPS correlation length as the external field h is decreased. Peaks at fields larger than inflection point represent genuine features of the system, while finite-D effects may generate spurious peaks at fields

smaller than the inflection point. Our findings corroborate the fact that the analysis of the running exponent is a useful diagnosis within the antiferromagnetic regime, away from the critical point. This proof-of-concept analysis shows the potential of the method put forward in Ref. [40] for future application of iPEPS, e.g., on questions of the stability of quantum spin liquids.

APPENDIX A: COMPARISON AMONG $U(1)$ CLASSES

First, we discuss the preparation of the initial $U(1)$-symmetric states for the optimization by imaginary-time evolution. We consider two scenarios of evolution by starting from simple $U(1)$-symmetric product states: a classical Néel antiferromagnet (*NEEL*) and a product state of singlets placed on the rungs of ladders (*VBS*). The imaginary-time evolutions were performed by using two-site simple update (SU) with the second-order Trotter approximation. To track the convergence of SU, we evaluate energy using corner-transfer matrix environments, with modest environment dimension $\chi \approx D^2$. Starting with the time step $\delta\tau = 0.02$, the state is evolved until an energy increase is observed, in which case the SU step is not performed and the time step is halved $\delta\tau \to \delta\tau/2$. The evolution ends once the time step becomes smaller than $\delta\tau = 10^{-8}$.

The $U(1)$ structure of the evolved *NEEL* and *VBS* states show slight variations in charges $\vec{v}_j^\gamma$. Moreover, depending on bond dimension D and α, the charges do not necessarily respect spatial symmetries of the model (1). For example, at $D = 5$ and 6 the charges on left ($j = l$) and right ($j = r$) bonds of tensors come out different. Then, we perform a further optimization of the *NEEL* and *VBS* states by using gradient descent and compare the resulting physical observables with the ones obtained from optimal states with identical charges $\vec{v}_j^\gamma$ for all bonds j), here denoted as *U1B* class. The results for the energy per site e and the local magnetization m are shown in Fig. 5. The data for $D = 3$ show that optimized *VBS* states have substantially worse energies than *NEEL* and *U1B* states. Instead, for $D > 3$, all these states have very similar energies, differences being at most of order 2×10^{-4}. The order parameter displays a similar behavior. A minor exception is represented by the $D = 4$ *VBS* case, which displays slight breaking of translation symmetry along the y axis even in the $\alpha = 1$ limit. In particular, the nearest-neighbor spin-spin correla-
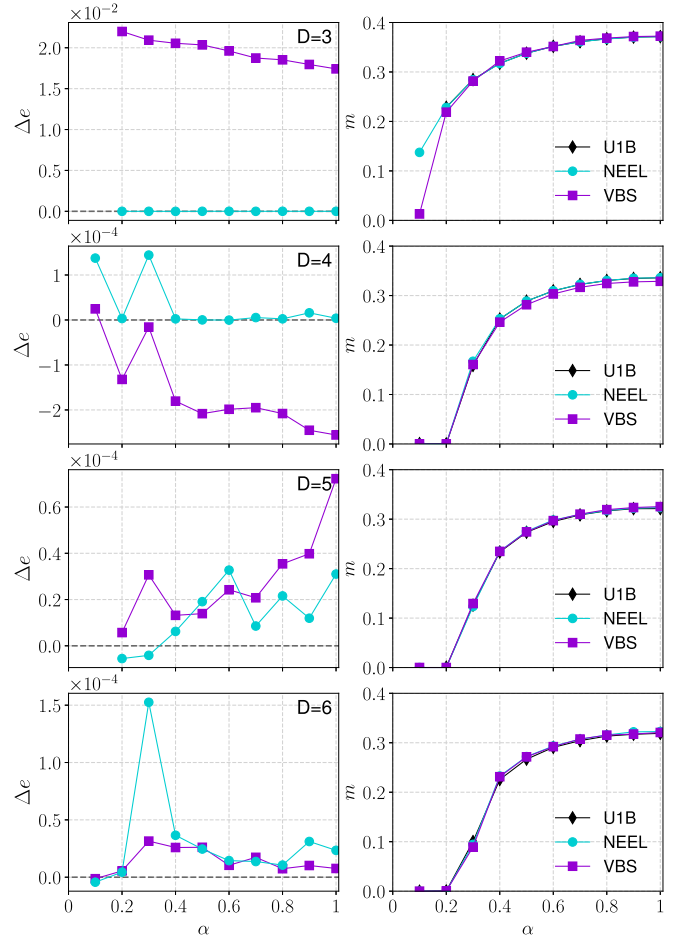

FIG. 5. Left panels: energy per site obtained optimizing *NEEL* and *VBS* states with respect to the one obtained within the *U1B* class, i.e., $\delta e = |e(NEEL) - e(U1B)|$ (circles) and $\delta e = |e(VBS) - e(U1B)|$ (squares) for different values of the bond dimension D. Right panels: magnetization m obtained from *NEEL*, *VBS*, and *U1B* states. Observables are evaluated at finite χ, i.e., $\chi = 71$ for $D = 3$, $\chi = 64$ for $D = 4$, $\chi = 50$ for $D = 5$, and $\chi = 72$.

tions show a staggered pattern with $\langle \vec{S}_{x,y} \cdot \vec{S}_{x,y+1} \rangle - \langle \vec{S}_{x,y+1} \cdot \vec{S}_{x,y+2} \rangle \approx 3 \times 10^{-4}$. Overall, the SU-evolved states provide reasonablly accurate initial states for the variational optimization of $U(1)$-symmetric iPEPS. Irrespective of the differences in the $U(1)$ charges, the final variational minima for different classes give quantitatively similar physical pictures.

APPENDIX B: SIZE SCALING ANALYSIS OF THE TRANSITION BY THE QMC TECHNIQUE

Here, we provide some standard details on locating the transition point α_c from QMC simulations. To estimate α_c, we have computed the spin stiffness ρ_s, defined using the winding number:

$$\rho_s = \frac{T}{2} \left\langle \sum_i \left(W_i^x\right)^2 + \left(W_i^y\right)^2 \right\rangle \tag{B1}$$
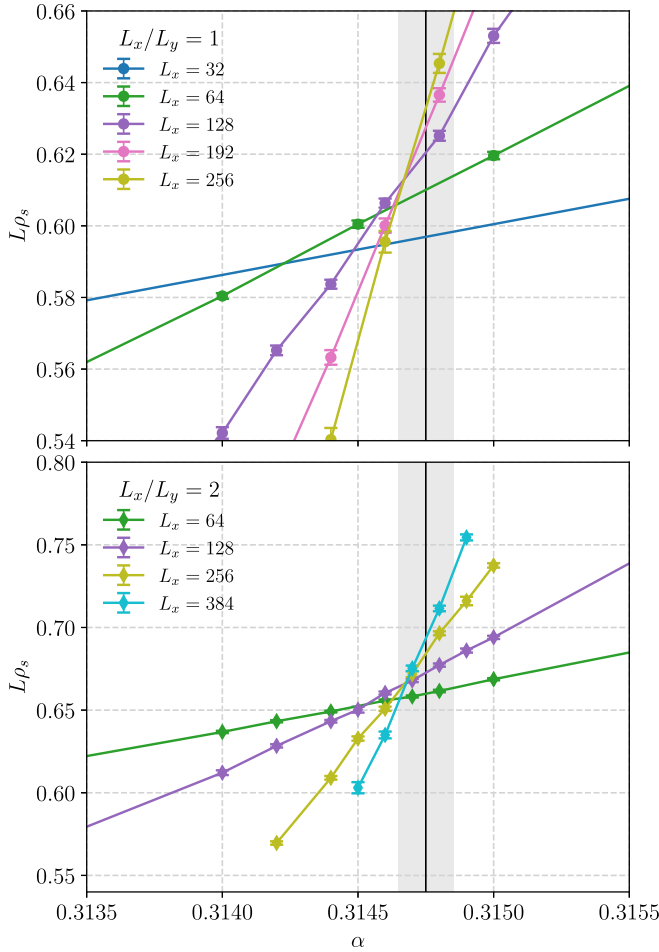
FIG. 6. QMC results for the scaling analysis of the spin stiffness ρ_s as a function of α for system with $L_x = L_y$ (upper panel) and $L_x = 2L_y$ (lower panel). The temperature has been chosen as $T = 1/(2L_x)$ to ensure convergence to the ground-state properties. The vertical black line and shaded area indicate the $\alpha_c = 0.31475(10)$ estimate and its uncertainty.
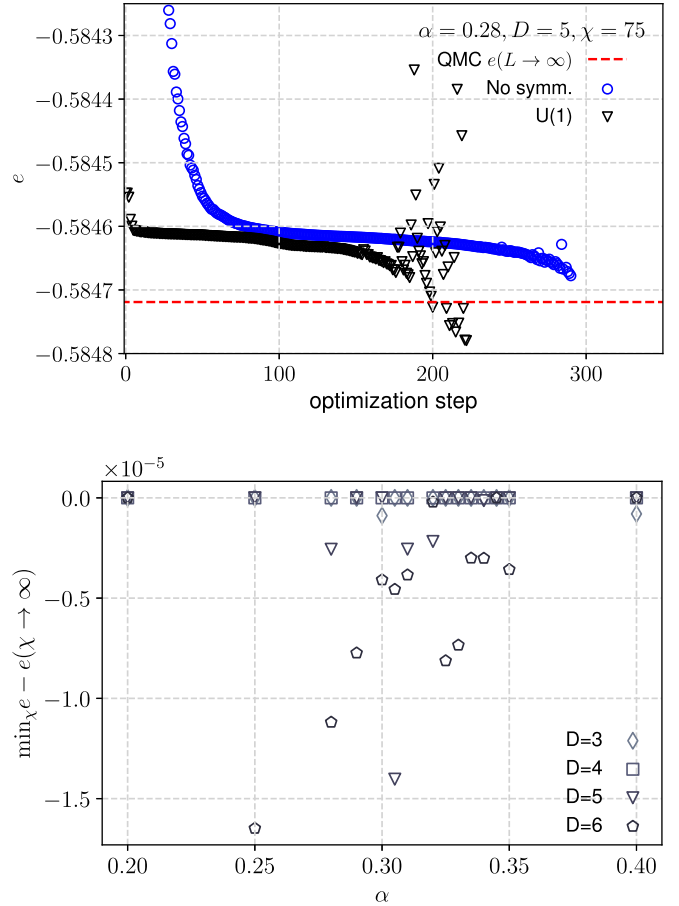

FIG. 7. Upper panel: example of optimizations without line search at $\alpha = 0.28$ (with $D = 5$ and $\chi = 75$) both with and without explicit $U(1)$ symmetry. Optimizations are initialized from $\alpha = 0.3$. The red line shows the comparison with QMC extrapolation. Lower panel: difference between thermodynamic estimate of the energy ($\chi \to \infty$ limit) and its minimal value for fixed environment dimension χ for optimized $U(1)$ symmetric states. The optimizations were done for $D = 3$, 4, 5, and 6 at $\chi_{\text{opt}} = 54$, 64, 100, and 108, respectively. In all cases, the line search was employed.

where i runs over loops in the space-time SSE configurations and the brackets denote the Monte Carlo average.

The results for different system sizes $L_x \times L_y$ are shown in Fig. 6. At criticality, the scaled spin stiffness $L_x\rho_s$ is constant (taking the dynamical exponent $z = 1$ at the transition), thus allowing to estimate the location of the transition at $\alpha_c = 0.31467(1)$. Note that the Binder cumulant crossing also leads to a similar critical value (data not shown). In addition, we have also checked that data collapse of ρ_s and magnetization are compatible with known exponents $\nu = 0.707$ and $\beta = 0.3689$.

APPENDIX C: INSTABILITY IN OPTIMIZATION

In the proximity of the critical point, we observed that performing the line search is crucial to obtain stable variational optimizations, especially for the cases with $D = 5$ and 6. In Fig. 7 (upper panel), we show typical cases done without line search, such that unstable regimes, with an erratic behavior of the energy, are obtained. The same kind of

problem appears both in simulations with or without the $U(1)$ symmetry.

When performing the optimization, we always work at constant environment bond dimension χ_{opt}. The states obtained in the erratic regime can show energies $e(\chi_{\text{opt}})$, which are lower than the reference QMC results. This is possible because the iPEPS thermodynamic estimate of energy, for which the variational principle holds, is obtained only in the limit of $\chi \to \infty$. When the line search is employed, it suppresses the erratic regime as the energy is not allowed to increase during the course of optimization. In this case, we asses the severity of this instability by comparing the lowest energies that are realized in the vicinity of χ_{opt} with the energy obtained from the $\chi \to \infty$ limit. The results for $D = 3, \ldots, 6$ and $0.2 \leqslant \alpha \leqslant 0.4$ are shown in Fig. 7 (lower panel). This behavior resembles overtraining, often encountered in the optimization of artificial neural networks, since the variational optimization of iPEPS does not directly optimize the thermodynamic estimate of energy $e(\chi \to \infty)$, but only its finite-χ

approximation. In the previous study of the J_1-J_2 model (using highly constrained single-site iPEPS *Anstaz* [25]), $e(\chi)$ was a monotonically decreasing function already from modest values of χ. Here, we instead observe that $e(\chi)$ attains shallow spurious minima, with depth at most $O(10^{-5})$, compared to corresponding $e(\chi \to \infty)$ thermodynamic estimates.

---

[1] S. R. White, Density Matrix Formulation for Quantum Renormalization Groups, Phys. Rev. Lett. **69**, 2863 (1992).

[2] A. Georges and G. Kotliar, Hubbard model in infinite dimensions, Phys. Rev. B **45**, 6479 (1992).

[3] S. R. White, D. J. Scalapino, R. L. Sugar, E. Y. Loh, J. E. Gubernatis, and R. T. Scalettar, Numerical study of the two-dimensional Hubbard model, Phys. Rev. B **40**, 506 (1989).

[4] S. Östlund and S. Rommer, Thermodynamic Limit of Density Matrix Renormalization, Phys. Rev. Lett. **75**, 3537 (1995).

[5] D. Perez-Garcia, F. Verstraete, M. Wolf, and J. I. Cirac, Matrix product state representations, Quantum Inf. Comput. **7**, 401 (2007).

[6] F. Verstraete and J. I. Cirac, Renormalization algorithms for quantum-many body systems in two and higher dimensions, arXiv:cond-mat/0407066.

[7] F. Verstraete and J. I. Cirac, Valence-bond states for quantum computation, Phys. Rev. A **70**, 060302(R) (2004).

[8] H. J. Liao, Z. Y. Xie, J. Chen, Z. Y. Liu, H. D. Xie, R. Z. Huang, B. Normand, and T. Xiang, Gapless Spin-Liquid Ground State in the $s = 1/2$ Kagome Antiferromagnet, Phys. Rev. Lett. **118**, 137202 (2017).

[9] P. Corboz and F. Mila, Tensor network study of the Shastry-Sutherland model in zero magnetic field, Phys. Rev. B **87**, 115144 (2013).

[10] P. Corboz, A. M. Läuchli, K. Penc, M. Troyer, and F. Mila, Simultaneous Dimerization and SU(4) Symmetry Breaking of 4-Color Fermions on the Square Lattice, Phys. Rev. Lett. **107**, 215301 (2011).

[11] P. Corboz, M. Lajkó, A. M. Läuchli, K. Penc, and F. Mila, Spin-Orbital Quantum Liquid on the Honeycomb Lattice, Phys. Rev. X **2**, 041013 (2012).

[12] J.-Y. Chen, S. Capponi, A. Wietek, M. Mambrini, N. Schuch, and D. Poilblanc, SU(3)$_1$ Chiral Spin Liquid on the Square Lattice: A View from Symmetric Projected Entangled Pair States, Phys. Rev. Lett. **125**, 017201 (2020).

[13] J.-Y. Chen, J.-W. Li, P. Nataf, S. Capponi, M. Mambrini, K. Totsuka, H.-H. Tu, A. Weichselbaum, J. von Delft, and D. Poilblanc, Abelian SU(N)$_1$ chiral spin liquids on the square lattice, Phys. Rev. B **104**, 235104 (2021).

[14] P. Corboz, T. M. Rice, and M. Troyer, Competing States in the t-J Model: Uniform d-Wave State versus Stripe State, Phys. Rev. Lett. **113**, 046402 (2014).

[15] B.-X. Zheng, C.-M. Chung, P. Corboz, G. Ehlers, M.-P. Qin, R. M. Noack, H. Shi, S. R. White, S. Zhang, and G. K.-L. Chan, Stripe order in the underdoped region of the two-dimensional Hubbard model, Science **358**, 1155 (2017).

[16] F. Pollmann, S. Mukerjee, A. M. Turner, and J. E. Moore, Theory of Finite-Entanglement Scaling at One-Dimensional Quantum Critical Points, Phys. Rev. Lett. **102**, 255701 (2009).

[17] B. Pirvu, G. Vidal, F. Verstraete, and L. Tagliacozzo, Matrix product states for critical spin chains: Finite-size versus finite-entanglement scaling, Phys. Rev. B **86**, 075117 (2012).

[18] M. M. Rams, P. Czarnik, and L. Cincio, Precise Extrapolation of the Correlation Function Asymptotics in Uniform Tensor Network States with Application to the Bose-Hubbard and XXZ Models, Phys. Rev. X **8**, 041033 (2018).

[19] B. Vanhecke, J. Haegeman, K. Van Acoleyen, L. Vanderstraeten, and F. Verstraete, Scaling Hypothesis for Matrix Product States, Phys. Rev. Lett. **123**, 250604 (2019).

[20] P. Corboz, Variational optimization with infinite projected entangled-pair states, Phys. Rev. B **94**, 035133 (2016).

[21] L. Vanderstraeten, J. Haegeman, P. Corboz, and F. Verstraete, Gradient methods for variational optimization of projected entangled-pair states, Phys. Rev. B **94**, 155123 (2016).

[22] H.-J. Liao, J.-G. Liu, L. Wang, and T. Xiang, Differentiable Programming Tensor Networks, Phys. Rev. X **9**, 031041 (2019).

[23] M. Rader and A. M. Läuchli, Finite Correlation Length Scaling in Lorentz-Invariant Gapless iPEPS Wave Functions, Phys. Rev. X **8**, 031030 (2018).

[24] P. Corboz, P. Czarnik, G. Kapteijns, and L. Tagliacozzo, Finite Correlation Length Scaling with Infinite Projected Entangled-Pair States, Phys. Rev. X **8**, 031031 (2018).

[25] J. Hasik, D. Poilblanc, and F. Becca, Investigation of the Néel phase of the frustrated Heisenberg antiferromagnet by differentiable symmetric tensor networks, SciPost Phys. **10**, 012 (2021).

[26] M. Matsumoto, C. Yasuda, S. Todo, and H. Takayama, Ground-state phase diagram of quantum Heisenberg antiferromagnets on the anisotropic dimerized square lattice, Phys. Rev. B **65**, 014407 (2001).

[27] J. Hasik and F. Becca, Optimization of infinite projected entangled pair states: The role of multiplets and their breaking, Phys. Rev. B **100**, 054429 (2019).

[28] T. Nishino, K. Okunishi, and M. Kikuchi, Numerical renormalization group at criticality, Phys. Lett. A **213**, 69 (1996).

[29] S. Singh, R. N. C. Pfeifer, and G. Vidal, Tensor network states and algorithms in the presence of a global U(1) symmetry, Phys. Rev. B **83**, 115125 (2011).

[30] H. C. Jiang, Z. Y. Weng, and T. Xiang, Accurate Determination of Tensor Network State of Quantum Lattice Models in Two Dimensions, Phys. Rev. Lett. **101**, 090603 (2008).

[31] W. H. Press, S. A. Teukolsky, W. T. Vetterling, and B. P. Flannery, *Numerical Recipes, The Art of Scientific Computing*, 3rd ed. (Cambridge University Press, Cambridge, 2007).

[32] M. M. Rams, G. Wójtowicz, and J. Hasik, YAST - Yet Another Symmetric Tensor: Differentiable linear algebra with block-sparse tensors, supporting abelian symmetries (2022), https://gitlab.com/marekrams/yast.

[33] J. Hasik and G. B. Mbeng, peps-torch: A differentiable tensor network library for two-dimensional lattice models (2020), https://github.com/jurajHasik/peps-torch.

[34] A. W. Sandvik, Stochastic series expansion method with operator-loop update, Phys. Rev. B **59**, R14157 (1999).

[35] A. F. Albuquerque, F. Alet, P. Corboz, P. Dayal, A. Feiguin, S. Fuchs, L. Gamper, E. Gull, S. Gürtler, A. Honecker, R. Igarashi, M. Körner, A. Kozhevnikov, A. Läuchli, S. R. Manmana, M. Matsumoto, I. P. McCulloch, F. Michel, R. M. Noack, G.

Pawłowski *et al.*, The ALPS project release 1.3: Open-source software for strongly correlated systems, J. Magn. Magn. Mater. **310**, 1187 (2007).

[36] B. Bauer, L. D. Carr, H. G. Evertz, A. Feiguin, J. Freire, S. Fuchs, L. Gamper, J. Gukelberger, E. Gull, S. Guertler, A. Hehn, R. Igarashi, S. V. Isakov, D. Koop, P. N. Ma, P. Mates, H. Matsuo, O. Parcollet, G. Pawłowski, J. D. Picon *et al.*, The ALPS project release 2.0: open source software for strongly correlated systems, J. Stat. Mech. (2011) P05001.

[37] H. Neuberger and T. Ziman, Finite-size effects in Heisenberg antiferromagnets, Phys. Rev. B **39**, 2608 (1989).

[38] D. S. Fisher, Universality, low-temperature properties, and finite-size scaling in quantum antiferromagnets, Phys. Rev. B **39**, 11783 (1989).

[39] K. Binder and D. P. Landau, Finite-size scaling at first-order phase transitions, Phys. Rev. B **30**, 1477 (1984).

[40] J. D'Emidio, A. A. Eberharter, and A. M. Läuchli, Diagnosing weakly first-order phase transitions by coupling to order parameters, arXiv:2106.15462.

[41] S. M. Chester, W. Landry, J. Liu, D. Poland, D. Simmons-Duffin, N. Su, and A. Vichi, Bootstrapping Heisenberg magnets and their cubic instability, Phys. Rev. D **104**, 105013 (2021).